

18. A. Dekker, G. Wensvoort, C. Terpstra, *Vet. Microbiol.* **47**, 317 (1995).
19. J. M. Daly et al., *J. Gen. Virol.* **77** (Pt. 4), 661 (1996).
20. A. S. Perelson, G. F. Oster, *J. Theor. Biol.* **81**, 645 (1979).
21. L. Edelstein, R. Rosen, *J. Theor. Biol.* **73**, 181 (1978).
22. D. J. Smith, S. Forrest, A. S. Perelson, in *Artificial Immune Systems and Their Applications*, D. Dasgupta, Ed. (Springer Verlag, Berlin, 1998), pp. 105–114.
23. D. J. Smith, S. Forrest, D. H. Ackley, A. S. Perelson, *Proc. Natl. Acad. Sci. U.S.A.* **96**, 14001 (1999).
24. J. Kruskal, *Psychometrika* **29**, 115 (1964).
25. R. Shepherd, *Hum. Factors* **5**, 33 (1963).
26. Newly sequenced HA1 domain accession numbers: AY660991–AY661211. Previously published HA1 domain accession numbers are in the supporting material.
27. C. A. Macken, H. Lu, J. Goodman, L. Boykin, in *Options for the Control of Influenza IV*, A. D. M. E. Osterhaus, N. Cox, A. W. Hampson, Eds. (Elsevier Science B.V., Amsterdam, 2001), pp. 103–106.
28. D. C. Wiley, I. A. Wilson, J. J. Skehel, *Nature* **289**, 373 (1981).
29. I. A. Wilson, J. J. Skehel, D. C. Wiley, *Nature* **289**, 366 (1981).
30. G. W. Both, M. J. Sleight, N. J. Cox, A. P. Kendal, *J. Virol.* **48**, 52 (1983).
31. A. J. Hay, V. Gregory, A. R. Douglas, Y. P. Lin, *Philos. Trans. R. Soc. London B. Biol. Sci.* **356**, 1861 (2001).
32. Single-letter abbreviations for the amino acid residues are as follows: I, Ile; K, Lys; N, Asn; and S, Ser.
33. J. R. Gog, B. T. Grenfell, *Proc. Natl. Acad. Sci. U.S.A.* **99**, 17209 (2002).
34. J. R. Gog, G. F. Rimmelzwaan, A. D. Osterhaus, B. T. Grenfell, *Proc. Natl. Acad. Sci. U.S.A.* **100**, 11143 (2003).
35. B. T. Grenfell et al., *Science* **303**, 327 (2004).
36. D. A. Lennette, in *Diagnostic Procedures for Viral, Rickettsial and Chlamydial Infections*, E. H. Lennette, D. A. Lennette, E. T. Lennette, Eds. (American Public Health Association, Washington, DC, 1995).
37. B. Korber et al., *Science* **288**, 1789 (2000).
38. We thank R. van Beek, W. Beyer, T. Bhattacharya, R. Bush, N. Cox, B. Grenfell, J. Gog, H. Gutowitz, A. Hay, R. Hightower, T. Jones, A. Tang, the contributors to

the WHO global influenza surveillance network, and the maintainers of the Influenza Sequence Database ([www.flu.lanl.gov](http://www.flu.lanl.gov)). We acknowledge the support of the Santa Fe Institute and the Dutch National Institute of Public Health and the Environment (RIVM). D.J.S. was supported by European Union grant QLRT-2001-01034. A.S.L. was supported by the U.S. Department of Energy, contract W-7405-ENG-36, under the Laboratory-Directed Research and Development program. R.A.M.F. is a fellow of the Royal Dutch Academy of Arts and Sciences.

## Supporting Online Material

[www.sciencemag.org/cgi/content/full/1097211/DC1](http://www.sciencemag.org/cgi/content/full/1097211/DC1)

Materials and Methods

Figs. S1 to S3

Table S1

References and Notes

26 February 2004; accepted 11 June 2004

Published online 24 June 2004;

[10.1126/science.1097211](https://doi.org/10.1126/science.1097211)

Include this information when citing this paper

# REPORTS

## Phase-Resolved Spectroscopy of Geminga Shows Rotating Hot Spot(s)

P. A. Caraveo,<sup>1\*</sup> A. De Luca,<sup>1</sup> S. Mereghetti,<sup>1</sup> A. Pellizzoni,<sup>1</sup>  
G. F. Bignami<sup>2,3,1</sup>

Isolated neutron stars are seen in x-rays through their nonthermal and/or surface thermal emissions. X-ray Multimirror Mission–Newton observations of the Geminga pulsar show a 43–electron volt spectrum from the whole neutron star surface, as well as a power-law component above 2 kiloelectron volts. In addition, we have detected a hot (170 electron volts) thermal emission from an ~60-meter-radius spot on the pulsar’s surface. Such a thermal emission, only visible at selected phase intervals, may be coming from polar hot spot(s), long thought to exist as a result of heating from magnetospheric accelerated particles. It may provide the missing link between the x-ray and gamma-ray emission of the pulsar.

Photons emitted by pulsars carry the signature of their production mechanisms as well as of the geometry of their emitting regions. Although neutron star physics is reflected in their photon spectra, geometrical constraints, such as viewing angles of rotational and magnetic axes, shape their observed light curves. Phase modulation takes place as different emitting regions are brought into view during the star rotation. Geometry can also influence source spectral shapes because of different emission mechanisms in different regions.

<sup>1</sup>Istituto di Astrofisica Spaziale e Fisica Cosmica, Consiglio Nazionale delle Ricerche, Via Bassini, 15–20133 Milano, Italy. <sup>2</sup>Centre d’Étude Spatiale des Rayonnements, Centre National de la Recherche Scientifique, Université Paul Sabatier, 9 Avenue du Colonel Roche, Toulouse, France. <sup>3</sup>Università di Pavia, Dipartimento Fisica Teorica e Nucleare, Via Ugo Bassi, 6 Pavia, Italy.

\*To whom correspondence should be addressed. E-mail: [pat@mi.iasf.cnr.it](mailto:pat@mi.iasf.cnr.it)

In spite of the potential interest of phase-resolved spectroscopy, the paucity of detected x-ray photons has made it impossible to apply this method to isolated neutron stars (INS), with the exception of the Crab pulsar (1). The European Photon Imaging Camera (EPIC) on XMM-Newton and Chandra can now provide an adequate harvest of time-tagged photons. However, phase-resolved spectroscopy is not yet commonly used. So far, it has been applied only to the Crab pulsar with Chandra (2) and to 1E1207-5209 with EPIC (3, 4). Although interesting, these sources represent specific and somewhat extreme cases among x-ray–emitting neutron stars. The Geminga pulsar, on the other hand, is often considered as archetypal (5) for middle-aged (350,000 years old) neutron stars, which emit x-rays mostly, but not solely, owing to their surface thermal emission. INS surface temperatures frequently yield radiation

in the x-ray domain (6), but keV photons can also be produced by energetic electrons in their strong magnetic fields. Geminga has the interesting characteristic of showing both thermal (7) and nonthermal processes to be at work in the sub-keV to several keV range (8, 9). With a photon number more than doubling all previous statistics, and with a wider (0.15 to 8 keV) spectral range, EPIC now offers the chance of a meaningful phase-resolved spectroscopy for Geminga.

XMM-Newton performed a 100-ksec exposure on 4 April 2002 with its three EPIC cameras. The two metal-oxide semiconductor (MOS) cameras (10) operated in “full frame” mode, while the positive-negative (pn) camera (11) operated in “small window” mode, ideal for accurate timing of source photons. After removing intervals with high particle background and correcting for dead time, we obtain a net exposure of 55.0 ksec for the pn camera and of 76.9 and 77.4 ksec for MOS1 and MOS2, respectively. The EPIC observation yielded a total of 76,850 photons in the energy range  $0.15 < E < 8$  keV, the majority of which (52,850 photons) are due to the pn detector. The MOS images have unveiled two tails of diffuse emission that are trailing Geminga and are well aligned with the source proper motion (12). Here, we present the analysis of the pn data, which were processed with the XMM-Newton Science Analysis Software (SAS version 5.4.1).

First, we have fitted the time-averaged, total source data (Fig. 1), using a combination of a black body and a power law. In view of the unsatisfactory result, we added a third component, both in the form of a black body and of a power law. The resulting  $\chi^2$  improved significantly, which suggests that Geminga’s spectrum indeed requires a three-component model.

Because an additional, steep power law cannot easily meet the constraints of the optical-to-UV part of the Geminga spectrum (13), we chose a second, hotter black-body component for the description of our time-averaged spectrum. To make our results comparable with the previous models (7–9), we adopted the  $N_{\text{H}}$  value obtained by Roentgen Satellite (ROSAT) (8) ( $N_{\text{H}} = 1.07 \times 10^{20}$ ). At the parallactic distance of 160 pc (14), the resulting parameters [ $T_1 = 43 \pm 1$  eV ( $4.8 \times 10^5$  K) from an  $8.6 \pm 1$  km radius surface;  $T_2 = 170 \pm 30$  eV ( $1.9 \times 10^6$  K) from a  $40 \pm 10$  m radius surface; power law photon index,  $1.7 \pm 0.1$ ] are similar to those derived by Halpern and Ruderman (7), and the index of the power law is identical to the latest model from Advanced Satellite for Cosmology and Astrophysics (ASCA) data (9). We note that, when extrapolated to  $E > 100$  MeV, such a power law is two orders of magnitude below the detected  $\gamma$ -ray flux (15).

We searched next for the best timing parameters. Standard epoch folding for our data set yielded a “best” period of  $0.2371012 \pm 1 \times 10^{-7}$  s. This agrees with the extrapolation of the Energetic Gamma Ray Experiment Telescope (EGRET) ephemeris (9), which gives a period of 0.2371012153 s, more accurate than our best value, owing to the much longer time span of the  $\gamma$ -ray data. To compare our light curves with the EGRET curves, we have adopted the extrapolated EGRET period. Light curves for three energy intervals, that is, 0.15 to 0.7 keV (dominated by cool black-body emission), 0.7 to 2 keV (hot black body), and 2 to 8 keV (power law), were drawn (Fig. 2).

Geminga’s light curves are different for different energies (9). The broad maximum at low energies is seen to change into two peaks at higher energies (0.7 to 2 keV and 2 to 8 keV): a prominent peak at phase  $\sim 0.5$  and a smaller peak at  $\sim 0.9$ . The minimum at phases 0.1 to 0.3, on the other hand, is common to all light curves. The pulsed fraction varies substantially as a function of energy, ranging from  $30.3 \pm 0.7\%$  at low energy, to  $54.5 \pm 2.4\%$  in the middle range, and back to  $33.2 \pm 4.5\%$  at higher energy. Our improved statistics do not confirm the very high pulsed fraction seen by (9) above 2 keV.

The  $\gamma$ -ray peaks occur at absolute pulsar phases 0.55 and 1.05, trailing our x-ray peaks by about 0.05 to 0.1 of phase. However, such a phase comparison (9) is entirely dominated by the uncertainty of the source spindown rate ( $\dot{P}$ ). Folding the EPIC data with  $\dot{P}$  values within  $\pm 2\sigma$  of the best EGRET fit, we obtain phases varying by about  $\pm 0.15$ . Such an error could shift our two x-ray peaks, separated by about 0.4 in phase, exactly between the two  $\gamma$ -ray peaks. However, a shift in the opposite direction would be equally probable.

The analysis done so far confirms and refines the results of two decades of x-ray

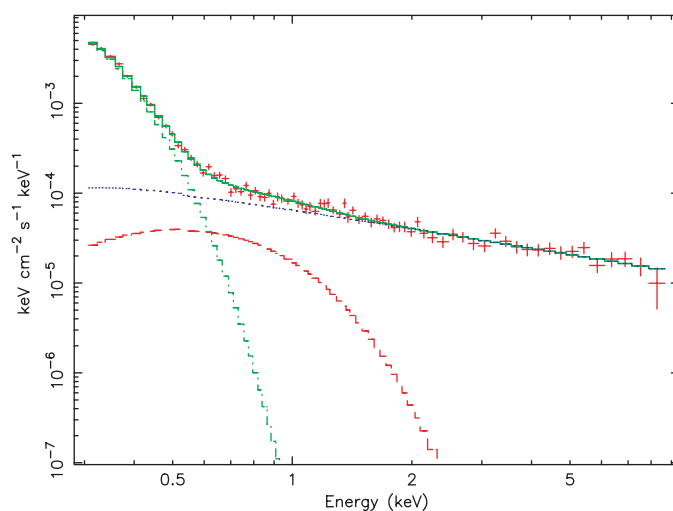
studies of Geminga, from the Einstein satellite (16) to the sequence of ROSAT and ASCA data (7–9). Spread among several ROSAT and ASCA observations, the pre-EPIC x-ray photons from Geminga number  $\sim 33,000$ . With  $\sim 53,000$  photons from a single observation, it makes sense to try phase-resolved spectroscopy.

Accordingly, we have divided the pulsar light curve into 10 phase intervals, also shown in Fig. 2, and for each of them a separate spectrum was drawn (Fig. 3A). Major spectral changes as a function of phase are apparent (Fig. 3A and movie S1). To better assess such a phase-dependent behavior, we also considered the deviations of each individual spectrum from the phase-averaged one (figs. S1 and S2). The biggest deviations occur in the medium interval ( $0.7 < E < 2$  keV), dominated by the hot black body. While spectra collected in intervals 1,

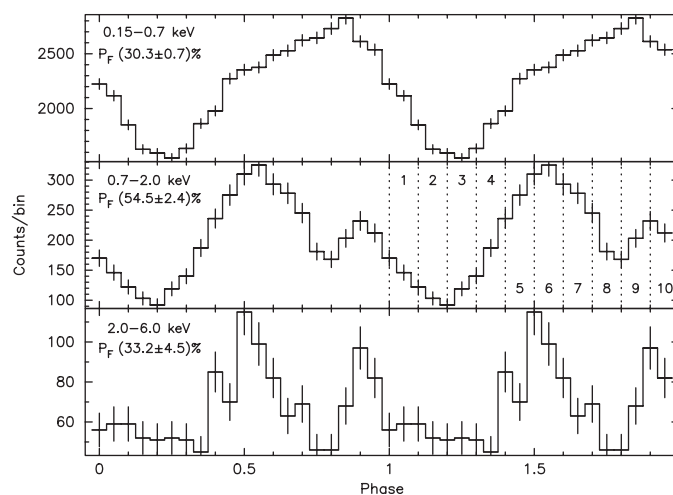
2, and 10 lack medium-energy photons, spectra 5, 6, and 7 (the x-ray prominent peak) show an overabundance of such photons, consistent with previous observations of a slightly softer main peak (9).

Individual spectra were then fitted by using the same three components that describe the average spectrum, with  $N_{\text{H}}$  fixed to the ROSAT value (8). First, the temperatures of both black bodies as well as the power-law index were allowed to vary. The resulting best fits showed that, within statistics, neither the two temperature values nor the power-law photon index had significant variations. Second, we repeated the fitting exercise, keeping temperatures and power-law index fixed while leaving their normalizations as free parameters. Figure 3B (with movie S1) gives the result of such a spectral fitting. For each phase interval, the three spectral components

**Fig. 1.** Time-averaged spectral distribution of all the Geminga pn data. Fits were carried out in the energy range 0.3 to 8 keV, where the instrument performances are best known. Background was subtracted after averaging over a suitable surrounding region. A combination of a single black body and a power law ( $T_{\text{bb}} = 44.5 \pm 1$  eV, covering a surface with a  $7 \pm 1$  km radius; power-law photon index  $1.90 \pm 0.05$ ;  $N_{\text{H}} < 1.4 \times 10^{20}$  cm $^2$ ) yields a  $\chi^2 = 1.35$  over 73 df. Adding a second black-body component to the spectral fit, we obtain:  $T_{\text{bb}1} = 43.8 \pm 1$  eV, radius of the emitting region  $7.5 \pm 1$  km;  $T_{\text{bb}2} = 185 \pm 20$  eV, radius of the emitting region  $33 \pm 10$  m; power-law photon index  $1.7 \pm 0.1$ ;  $N_{\text{H}} < 1.2 \times 10^{20}$  cm $^2$ , yielding a  $\chi^2$  1.21 over 71 df. With an F test, such a fit improvement has a chance occurrence probability of  $5 \times 10^{-3}$ . The corresponding observed flux is  $1.1 \times 10^{-12}$  erg/cm $^2$ /s (0.3 to 8 keV), and the bolometric luminosities of the three components are  $L_{\text{bb}1} = 2.6 \times 10^{31}$  erg/s;  $L_{\text{bb}2} = 1.5 \times 10^{29}$  erg/s;  $L_{\text{pl} (2-8 \text{ keV})} = 7.7 \times 10^{29}$  erg/s.



**Fig. 2.** Background subtracted light curves, obtained for three energy ranges, with a period of 0.2371012153 s, extrapolated from the EGRET ephemeris (9). Two phases are shown for clarity. The 10 phase intervals used for the time-resolved spectroscopy are also indicated. Pulsed fractions have been computed as the ratio between the counts above the minimum of each light curve and the total number of counts detected in each energy interval.



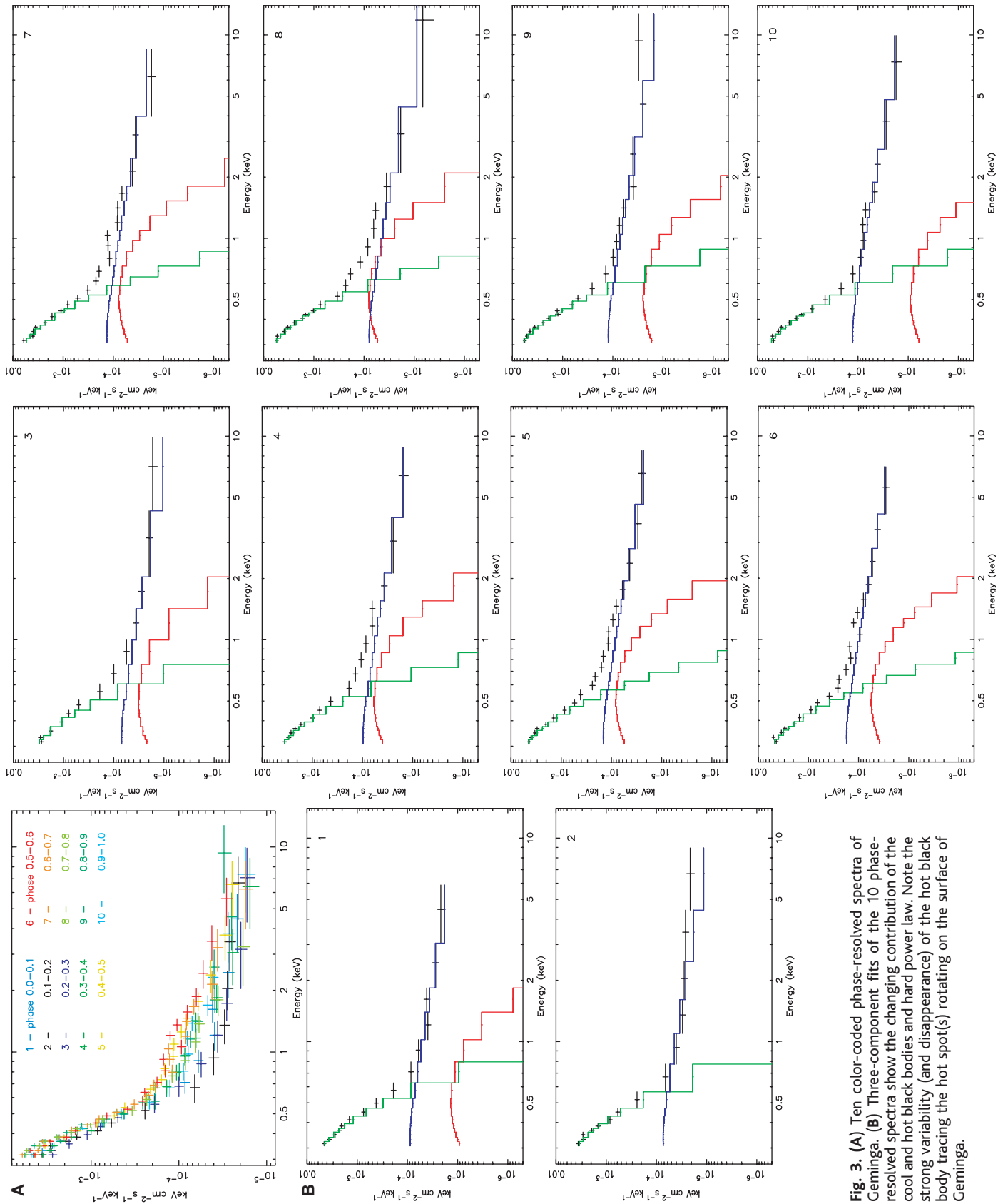


**Fig. 3. (A)** Ten color-coded phase-resolved spectra of Geminga. **(B)** Three-component fits of the 10 phase-resolved spectra show the changing contribution of the cool and hot black bodies and hard power law. Note the strong variability (and disappearance) of the hot black body tracing the hot spot(s) rotating on the surface of Geminga.

are shown. The phase-resolved spectra show that we need a second, hotter black body, because its contribution, although strongly phase dependent, is unavoidable for a satisfactory fit to all spectra except spectrum 2, for which the hot black-body component is seen to vanish. This particular phase interval is well fit with just a single cool black body and a power law. The values derived for the emitting surfaces of the two black bodies and for the power-law normalization vary as a function of the pulsar phase, albeit with different time evolutions (Fig. 4).

While the variations of the emitting area of the two black bodies could be described as sinusoidal, the variation of the nonthermal contribution follows a different, double-peaked pattern. We note that the emitting region(s) responsible for the nonthermal emission are located somewhere in the neutron star magnetosphere, whereas the thermal emissions are coming, most probably, from close to the neutron star surface. Thus, the lack of phase correlation between the two thermal emissions is more surprising, and revealing, than the phase behavior of the higher energy photons.

While the cool black body covers a sizable fraction of the neutron star surface, the hotter one comes from a minute fraction of it. Its inferred dimension (up to 60-m radius) is compatible with the expected extension of the polar cap for a spinning neutron star like Geminga (nominal value of the “dipole” polar cap radius,  $R \sqrt{\frac{R\Omega}{c}} \sim 300$  m, where  $R$  is the 10-km star radius,  $\Omega$  is Geminga’s angular velocity, and  $c$  is the velocity of light), especially considering possible geometrical effects (17). A nearly aligned rotator viewed at high inclination could easily yield a geometrical reduction of  $\sim 10$  between the nominal value and our apparent spot radius.

Thus, we propose the hot black-body emission to come from the polar cap(s) of the mag-

netized neutron star, heated by particles accelerated in the pulsar magnetosphere. The same process responsible for the copious  $\gamma$ -ray emission of Geminga would thus also be responsible for the appearance of the hot spots on its surface (7). Such a mechanism has been posited to exist for  $\gamma$ -ray pulsars (18, 19).

The inferred bolometric luminosity of Geminga’s polar cap(s) is  $1.5 \times 10^{29}$  erg/sec. It is a value compatible with the predictions of (20) for polar cap heating based on inverse Compton scattering (ICS) pair fronts. Because heating from return curvature radiation would exceed our measured luminosity by at least two orders of magnitude (7, 20), some mechanism must prevent it. Geminga is the only  $\gamma$ -ray pulsar close to the so-called death line, where pulsars no longer produce pairs by curvature radiation (20), and its age and evolution may help explain why the heating is diminished.

We cannot determine how many hot spots are at one polar cap or whether hot spots occur at both caps. Three-dimensional modeling, taking gravitational light bending into account, is needed to determine the hot-spot distribution. The visibility of small hot spot(s) for the majority of the pulsar period suggests a nearly aligned rotator seen at high inclination.

The sinusoidal evolution of the cooler black body favors a single extended polar region, warmer than the rest of the star because of higher thermal conductivity parallel to the magnetic field (21). Such a geometry would yield a correlated behavior between the two black-body emissions. Instead, the lack of correlation in the phase evolution of the cool and hot black-body emissions from the surface of Geminga argues against such an interpretation, unless different beaming mechanisms are invoked for different emitting regions. Alternatively, the cool black body could come from a vast “continent” on the neutron star equatorial surface, where multipole mag-

netic fields could play a role (22). Cold black-body radiation could also arise from surface x-rays reprocessed within a blanket formed above vast star regions by electron-positron ( $e^+e^-$ ) pairs created on closed field lines (19). The double-peaked structure of photons  $>2$ keV argues against the single-pole hypothesis. However, emitting regions higher up in the magnetosphere, at the rim of a single cone, could yield a two-peak nonthermal light curve (23). Alternatively, the off-center dipole proposed by (7) could provide a viable solution.

In a few years, by operating XMM-Newton in coordination with Astrorivelatore Gamma a Immagini Leggero (AGILE) (24) and the Gamma Ray Large Area Space Telescope (GLAST) (25), it will be possible to exploit the physical link now seen between  $\gamma$ -rays, pulsar energetic particles, return current, and polar hot spots to gain deeper insight into the complex phenomenology of Geminga.

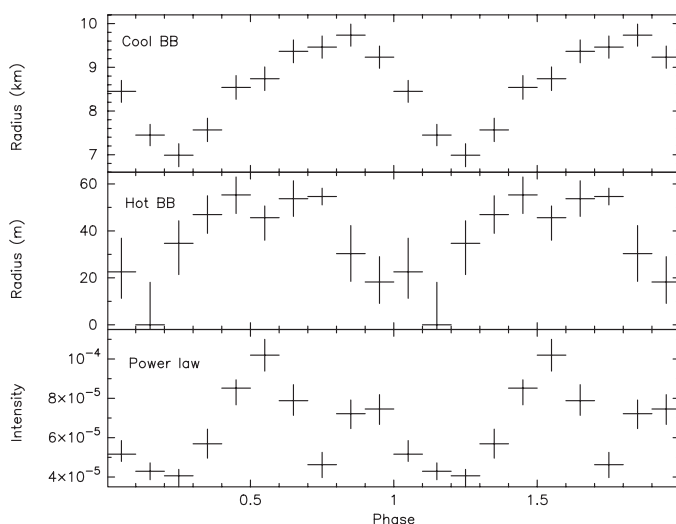
References and Notes

1. H. S. Pravdo et al., *Astrophys. J.* **491**, 808 (1997).
2. M. C. Weisskopf et al., *Astrophys. J.* **601**, 1050 (2004).
3. G. F. Bignami, P. A. Caraveo, A. De Luca, S. Mereghetti, *Nature* **423**, 725 (2003).
4. A. De Luca et al., *Astron. Astrophys.* **418**, 625 (2004).
5. G. F. Bignami, P. A. Caraveo, *Ann. Rev. Astron. Astrophys.* **34**, 331 (1996).
6. V. M. Kaspi, M. S. E. Roberts, A. K. Harding, in *Compact Stellar X-ray Sources*, W. H. G. Lewin and M. van der Klis, Eds., in press. Available at <http://arxiv.org/abs/astro-ph/0402136>.
7. J. P. Halpern, M. Ruderman, *Astrophys. J.* **415**, 286 (1993).
8. J. P. Halpern, F. Y.-H. Wang, *Astrophys. J.* **477**, 905 (1997).
9. M. S. Jackson, J. P. Halpern, E. V. Gotthelf, J. R. Mattox, *Astrophys. J.* **578**, 935 (2002).
10. M. Turner et al., *Astron. Astrophys.* **365**, L27 (2001).
11. L. Strüder et al., *Astron. Astrophys.* **365**, L18 (2001).
12. P. A. Caraveo et al., *Science* **301**, 1345 (2003).
13. R. P. Mignani, P. A. Caraveo, G. F. Bignami, *Astron. Astrophys.* **332**, L37 (1998).
14. P. A. Caraveo et al., *Astrophys. J.* **461**, L1 (1996).
15. H. Mayer-Hasselwander et al., *Astrophys. J.* **421**, 276 (1994).
16. G. F. Bignami, P. A. Caraveo, R. C. Lamb, *Astrophys. J.* **272**, L9 (1983).
17. D. Psaltis, F. Özel, S. Dedeo, *Astrophys. J.* **544**, 390 (2000).
18. K. S. Cheng, L. Zhang, *Astrophys. J.* **515**, 337 (1999).
19. F. Y.-H. Wang, M. Ruderman, J. P. Halpern, T. Zhu, *Astrophys. J.* **498**, 373 (1998).
20. A. K. Harding, A. G. Muslimov, *Astrophys. J.* **568**, 862 (2002).
21. G. Greenstein, G. J. Hartke, *Astrophys. J.* **271**, 283 (1983).
22. D. Page, Yu. A. Shibano, V. E. Zavlin, *Astrophys. J.* **451**, L21 (1995).
23. J. K. Daugherty, A. K. Harding, *Astrophys. J.* **429**, 325 (1994).
24. M. Tavani et al., *SPIE*, **4851**, 1151 (2003). <http://agile.mi.iasf.cnr.it>.
25. P. F. Michelson, *SPIE*, **4851**, 1144 (2003). [www-glast.stanford.edu](http://www-glast.stanford.edu).
26. The XMM-Newton data analysis is supported by the Italian Space Agency (ASI). A.D.L. acknowledges an ASI fellowship.

Supporting Online Material

[www.sciencemag.org/cgi/content/full/305/5682/376/DC1](http://www.sciencemag.org/cgi/content/full/305/5682/376/DC1)  
 Figs. S1 and S2  
 Movie S1

**Fig. 4.** Phase evolution of the three components of Fig. 3B. The variations of the apparent surfaces of the two black-body (BB) emitting regions as well as the nonthermal flux are shown. (Top) Phase evolution of the radius (in km) of the emitting area of the 43-eV black body. (Middle) Phase evolution of the radius (in m) of the emitting area of the 170-eV black body. (Bottom) Phase evolution of the power-law flux at 1 keV.



25 February 2004; accepted 24 May 2004